

# Influence of Cloud–Radiative Forcing on Tropical Cyclone Structure

YIZHE PEGGY BU AND ROBERT G. FOVELL

*Department of Atmospheric and Oceanic Sciences, University of California, Los Angeles,  
Los Angeles, California*

KRISTEN L. CORBOSIERO

*Department of Atmospheric and Environmental Sciences, University at Albany,  
State University of New York, Albany, New York*

(Manuscript received 25 August 2013, in final form 20 November 2013)

## ABSTRACT

The authors demonstrate how and why cloud–radiative forcing (CRF), the interaction of hydrometeors with longwave and shortwave radiation, can influence tropical cyclone structure through “semi idealized” integrations of the Hurricane Weather Research and Forecasting model (HWRF) and an axisymmetric cloud model. Averaged through a diurnal cycle, CRF consists of pronounced cooling along the anvil top and weak warming through the cloudy air, which locally reverses the large net cooling that occurs in the troposphere under clear-sky conditions. CRF itself depends on the microphysics parameterization and represents one of the major reasons why simulations can be sensitive to microphysical assumptions.

By itself, CRF enhances convective activity in the tropical cyclone’s outer core, leading to a wider eye, a broader tangential wind field, and a stronger secondary circulation. This forcing also functions as a positive feedback, assisting in the development of a thicker and more radially extensive anvil than would otherwise have formed. These simulations clearly show that the weak (primarily longwave) warming within the cloud anvil is the major component of CRF, directly forcing stronger upper-tropospheric radial outflow as well as slow, yet sustained, ascent throughout the outer core. In particular, this ascent leads to enhanced convective heating, which in turn broadens the wind field, as demonstrated with dry simulations using realistic heat sources.

As a consequence, improved tropical cyclone forecasting in operational models may depend on proper representation of cloud–radiative processes, as they can strongly modulate the size and strength of the outer wind field that can potentially influence cyclone track as well as the magnitude of the storm surge.

## 1. Introduction

For some time, we have known that assumptions within microphysical parameterizations (MPs), which account for the creation, evolution, and destruction of hydrometeors, can dramatically influence tropical cyclone (TC) intensity (e.g., Lord et al. 1984; Braun and Tao 2000; Wang 2002; Zhu and Zhang 2006). Fovell and Su (2007) were among the first to show that cloud processes could materially influence TC motion over periods as short as 2 days. Using “semi idealized” modeling, defined presently, Fovell et al. (2009) demonstrated that

MPs tend to generate different storm structures, particularly with regard to the azimuthally averaged winds in the TC outer-core region, located 200 km or more from the center. These outer winds can influence motion via the “beta drift” (e.g., Holland 1983; Fiorino and Elsberry 1989). Indeed, Cao et al. (2011) found that the outer wind structures that evolved in their simulations depended much less on the initial condition than on the model physics being employed.

This sensitivity to the MP, however, emerged owing to how hydrometeors in different schemes interacted with radiative processes. That was the finding of Fovell et al. (2010a), who demonstrated that the motion and structural variation in their MP ensemble disappeared when clouds were made transparent to radiation in their semi-idealized simulations employing the Weather Research and Forecasting model’s (WRF’s) Advanced Research

---

*Corresponding author address:* Dr. Robert Fovell, Department of Atmospheric and Oceanic Sciences, University of California, Los Angeles, 405 Hilgard Ave., Los Angeles, CA 90096-1565.  
E-mail: rfovell@ucla.edu

TABLE 1. Moist runs with HWRf.

Case	MPs	Radiation scheme	Clear-sky forcing	CRF	Description
CRF-on	Thompson	RRTMG	On	On	Control run
CRF-off	Thompson	RRTMG	On	Off	Clouds transparent to radiation
CRF > 0	Thompson	RRTMG	On	On	Only positive CRF retained
CRF < 0	Thompson	RRTMG	On	On	Only negative CRF retained
GFDL	Thompson	GFDL	On	—	Operational HWRf radiation scheme used

WRF (ARW) core. MP schemes differ with respect to the amounts and relative distributions of hydrometeors, such as cloud ice, snow, cloud droplets, etc. (Fovell et al. 2010b). These particles have different effective sizes that determine how they interact with longwave (LW) and shortwave (SW) radiation (e.g., Dudhia 1989).

Herein, we demonstrate how and why cloud–radiative forcing (CRF), the modulation of atmospheric radiation owing to hydrometeors, can influence tropical cyclones. The specific focus is on storm structure, emphasizing the strength of the outer-core winds. We will show that the CRF results in pronounced LW cooling along the anvil top that is partially countered by the absorption of SW radiation during the daytime, as well as weak LW warming within the cloudy area, which removes (and actually reverses) the fairly large LW cooling that occurs in the troposphere under clear-sky conditions. It is the weak in-cloud warming that emerges as the most important component of CRF. The *direct* effects of CRF are to encourage stronger upper-tropospheric radial outflow as well as gentle yet sustained ascent through the outer-core region. CRF’s *indirect* effects are to enhance convective activity in the outer core and increase the size of the TC eye, shifting the radius of maximum winds (RMW) radially outward. The combined impact of CRF is to foster a broader storm circulation, other factors being equal.

The organization of this paper is as follows. The models employed in this study are described in section 2. Section 3 demonstrates the influence of CRF in the Hurricane WRF model (HWRf). Moist and dry simulations with a simplified axisymmetric model are used to demonstrate how and why cloud–radiative forcing influences TC structure in section 4, which concludes with confirmation using HWRf. The final section presents the summary.

## 2. Models and experimental designs

Some of the simulations (Table 1) examined herein were made using the Hurricane WRF (Gopalakrishnan et al. 2012), which is based on the WRF’s Nonhydrostatic Mesoscale Model (NMM) core (Janjić 2003). Specifically, we used a preimplementation version of the 2013 HWRf

that has been modified to incorporate the Thompson et al. (2008) microphysical parameterization. Thanks to G. Thompson of the National Center for Atmospheric Research, this MP scheme is now “fully connected” to the Rapid Radiative Transfer Model for General Circulation Models (RRTMG) (Iacono et al. 2008) LW and SW radiation schemes in HWRf. This means that the microphysics scheme now passes particle size information to the radiation parameterization, resulting in more precise CRF computations. Previously, only hydrometeor mass was shared with the radiation scheme, which internally made assumptions regarding particle sizes. In HWRf, CRF in the RRTMG package is controlled by the namelist parameter “icloud.”

These experiments are semi-idealized in the sense that our implementation employed the “real data” version of the model, and were guided by the operational configuration, but were dramatically simplified to exclude land, employ a uniform and constant sea surface temperature (SST), and start with a horizontally homogeneous tropical sounding (modified from Jordan 1958; see Fovell et al. 2010a) without any mean flow. Accordingly, we adopted the operational HWRf domain design used during the 2012 hurricane season, consisting of three telescoping domains (denoted D1–D3) with horizontal grid spacings of 27, 9, and 3 km (Fig. 1), and model time steps of 45, 15, and 5 s, respectively. We also adopted some of the model physics used operationally, such as the simplified Arakawa–Schubert (SAS) cumulus parameterization (only in the 27- and 9-km domains after 24 h)<sup>1</sup> and the Global Forecast System (GFS) planetary boundary layer (PBL) scheme.

A synoptic-scale virtual temperature perturbation was inserted into this initialization that subsequently organizes into a TC [see Cao et al. (2011), and references therein, for more background information on this “bubble” procedure]. During the first 24 h, the initial perturbation evolved into a coherent vortical circulation of tropical storm strength, as determined by the largest

<sup>1</sup>The “bubble” initialization, described subsequently, employs a cumulus scheme in all domains for the first 24 h. See Cao et al. (2011).

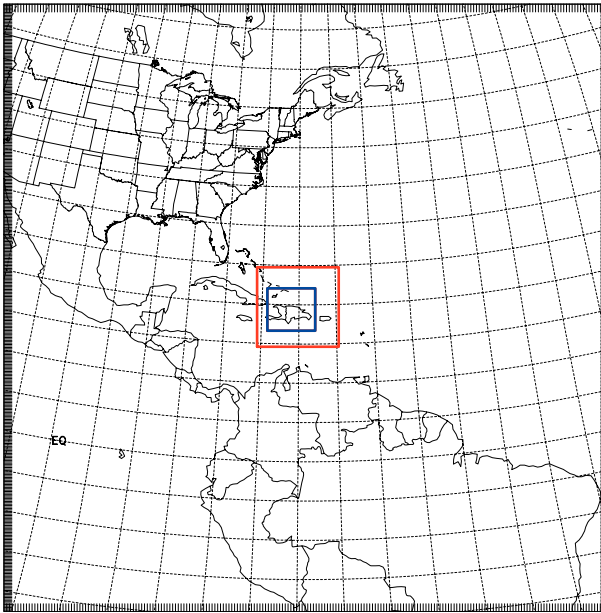


FIG. 1. Domain configuration for the HWRf simulations. The outer (27 km) domain is approximately an  $80^\circ \times 80^\circ$  square, while the inner nests are about  $11^\circ \times 10^\circ$  and  $6^\circ \times 5^\circ$  for the 9-km and 3-km domains, respectively. Although land areas are plotted to provide a sense of scale, there is no land in these semi-idealized simulations.

tangential wind speed at 10 m MSL. All HWRf simulations spanned 4 days; over this period, issues relating to the lateral boundaries do not emerge. Composite model fields were constructed for the fourth day in a vortex-following fashion, averaging over one full diurnal cycle.

However, our control configuration deviates from the HWRf operational setup in several important aspects. Our HWRf is not coupled to an ocean model, and the SST is held fixed at  $29.5^\circ\text{C}$ . While the inner two domains were enlarged for the 2013 season, we have retained the 2012 dimensions (see Fig. 1). There are important differences with respect to model integration and physical parameterizations as well. For reasons of efficiency, the operational HWRf does not call the MP and PBL schemes every time step, but our simulations do, which

is the standard practice with ARW. As in past years, the 2013 operational version of HWRf uses a tropical variant of the Ferrier et al. (2002) MP scheme and a radiation parameterization originating in the Geophysical Fluid Dynamics Laboratory (GFDL) (see Gopalakrishnan et al. 2012) model. This study is limited to the Thompson MP with the RRTMG and GFDL schemes. At present, the GFDL radiation package is not fully connected to any microphysics scheme.

Supporting moist and dry simulations were made using the G. Bryan Cloud Model 1 (CM1) (Bryan and Fritsch 2002; Bryan and Rotunno 2009) in axisymmetric mode, representing an  $f$  plane at  $20^\circ\text{N}$ . These runs commenced with the Rotunno and Emanuel (1987) sounding and utilized a 5-km radial grid spacing in a domain 8000 km wide and 24.7 km deep. The vertical grid spacing was 625 m. In the moist simulations (Table 2), a version of the Thompson MP was used but was not fully connected to the Goddard radiation (Chou and Suarez 1994) package. Those runs were initialized with a weak initial vortex and generally integrated for 16 days and composites were created by averaging between days 9 and 12. The dry simulations (Table 3) were averaged over the first 4 days.

### 3. Influence of CRF on HWRf storm structure

In this section, the structures of the HWRf storms are examined using temporally averaged fields, emphasizing the Thompson/RRTMG schemes with and without CRF. All composites were computed in a vortex-following manner over day 4, thereby spanning one full diurnal cycle. For the azimuthally averaged plots, it should be borne in mind that these TCs possessed substantial asymmetry.

That asymmetry can be seen in the vertically averaged vertical velocity fields, which reveal that both Thompson/RRTMG TCs had inner-core ascent concentrated east of the eye (Fig. 2). Although the runs commenced with neither mean flow nor shear, deep tropospheric vertical shear developed owing to the beta effect (cf.

TABLE 2. Moist runs with CM1.

Case	MPs	Radiation scheme	Clear-sky forcing	CRF	Description
CRF-on	Thompson	Goddard	On	On	Control run
CRF-off	Thompson	Goddard	On	Off	Clouds transparent to radiation
CRF-fixed	Thompson	Goddard	On	Fixed	Temporally averaged CRF of CRF-on used
Outflow $q_x = 0$	Thompson	Goddard	On	As CRF-fixed	No condensate permitted in the outflow
Outflow $V_t = 0$	Thompson	Goddard	On	As CRF-fixed	No hydrometeor terminal velocity in outflow
CRF $> 0$	Thompson	Goddard	On	As CRF-fixed	Only positive CRF retained
CRF $< 0$	Thompson	Goddard	On	As CRF-fixed	Only negative CRF retained

TABLE 3. Dry runs with CM1.

Case	MPs	Radiation scheme	Clear-sky forcing	CRF	Imposed forcing
Dry CRF	—	—	None	Fixed	Temporally averaged CRF of moist CRF-on run
Dry CRF > 0	—	—	None	Fixed	Positive component of temporally averaged CRF of moist CRF-on run
Dry CRF < 0	—	—	None	Fixed	Negative component of temporally averaged CRF of moist CRF-on run
Outer heating	—	—	None	None	Positive component of temporally averaged microphysical diabatic heating difference field between CM1 CRF-on and CRF-off runs

Bender 1997). The beta shear vector was directed southeastward (not shown), enhancing inner-core convective activity on the downshear to downshear-left side, consistent with observations and theory (e.g., Frank and Ritchie 1999; Corbosiero and Molinari 2002). Similar structures were reported in Fovell et al. (2010a), whose simulations employed the same initial condition with ARW.

Of the two model storms, the CRF-on TC (Fig. 2a) has clearly developed a larger amount of convective activity beyond the eyewall region. Part of this activity is the prominent zone of enhanced ascent south of the storm, which originates on the eastern flank and curves

anticyclonically outward. This resembles the “principal rainband” in the Houze (2010) schematic (his Fig. 30), a feature that tends to be “more or less stationary relative to the storm” (see also Willoughby et al. 1984) and thus (in contrast to individual convective cells) survives the averaging process. There is a suggestion of a principal rainband structure in the CRF-off simulation as well (Fig. 2b), but it is far less extensive.

The CRF-on storm also developed a significantly broader wind field at 10 m MSL, extending radially outward from a relatively wider eye. The radius of its 34-kt (about  $17.5 \text{ m s}^{-1}$ ) wind is 80 km farther outward, making it over 70% wider than in the CRF-off case (Fig. 3).

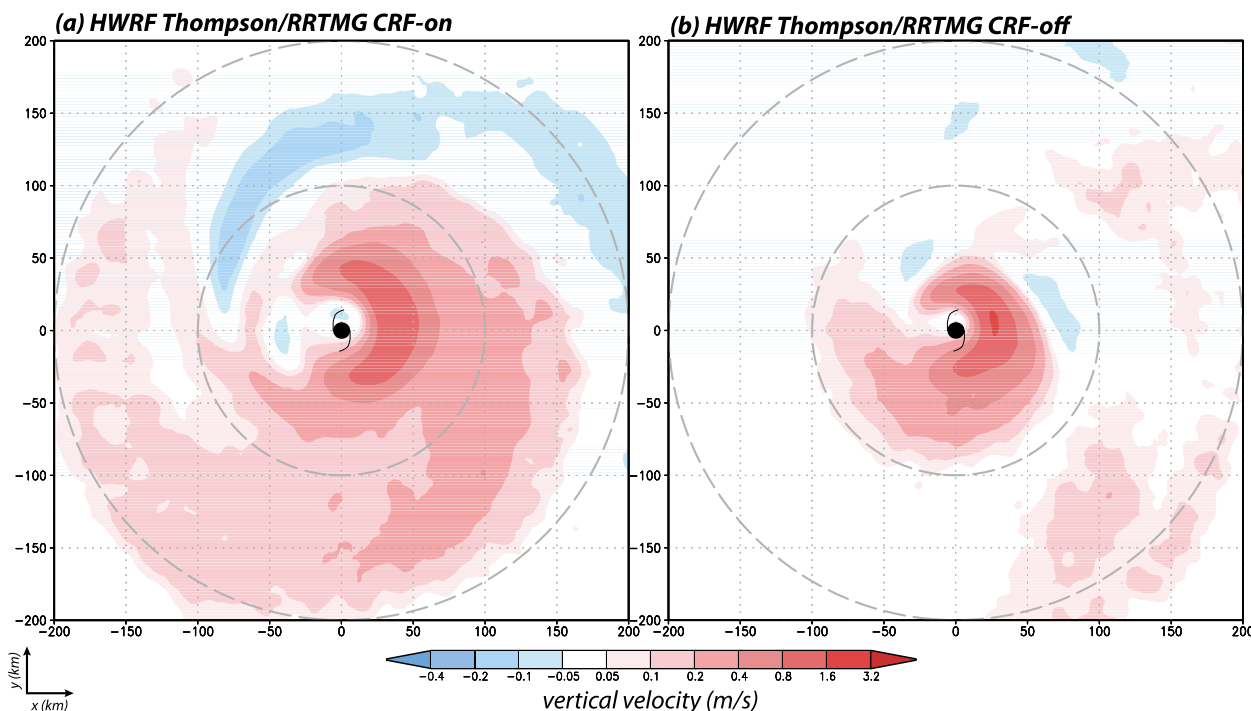


FIG. 2. Vertical velocity averaged from the surface to 500 hPa (mass weighted) from HWRP simulations using Thompson MP and RRTMG radiation for the (a) CRF-on and (b) CRF-off cases. Fields were averaged in a vortex-following sense over day 4 of the simulations. The  $400 \times 400 \text{ km}^2$  square portion of D2 is shown, as are 100- and 200-km range rings. The top of the figure represents north.

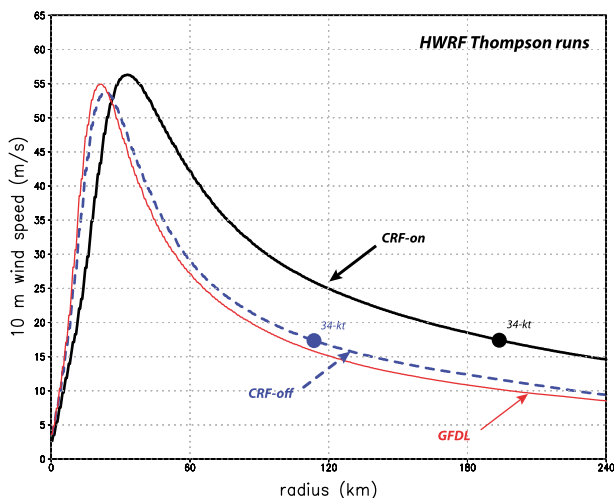


FIG. 3. Radial profiles of the azimuthally averaged 10-m wind speed from the HWRf day-4 composite, computed from D3. The Thompson/RRTMG CRF-on and CRF-off simulations are shown, along with a Thompson simulation made using the HWRf GFDL radiation scheme. Radii of the 34-kt ( $17.5 \text{ m s}^{-1}$ ) wind are indicated.

The wind field expansion is a consequence of permitting hydrometeors to modulate the radiative tendencies, and not the recently improved MP-radiation connectivity. Simulations using the original, partially connected RRTMG scheme with CRF active had nearly identical storm structures (not shown). Note also that the Thompson simulation with the GFDL radiation scheme is quite similar to the RRTMG CRF-off storm. We will soon see that the GFDL scheme implemented in HWRf evinces little to no cloud-radiative forcing.

This CRF-on TC broader circulation extends through much of the troposphere (Fig. 4), as demonstrated by the highlighted  $20 \text{ m s}^{-1}$  tangential wind contour. The CRF-on storm's secondary circulation was more intense, with stronger outflow in the upper troposphere as well as faster inflow near the surface (Fig. 4c). The largest differences with respect to tangential velocity resided in the lower troposphere, below the 5-km level. The CRF-on TC also possessed a thicker, more radially extensive condensate field, as revealed by the azimuthally averaged total condensate distribution (Fig. 5), with two separate regions of enhanced cloud content, separated by the melting level (roughly 4.5 km MSL). The negative values in the difference field (Fig. 5c) near the center reflect the narrower eye of the CRF-off TC.

The potential temperature tendency ( $\text{K h}^{-1}$ ) owing to net radiation (hereafter referred to as “radiative forcing”) for the CRF-on simulation (Fig. 5a) reveals the existence of prominent cooling along the cloud top, with warming within the cloud, largest at the outer region

where the cloud thickness is smaller. The CRF-off storm (Fig. 5b) possesses only clear-sky forcing, which outside the eye is smaller than the contour intervals selected ( $0.05 \text{ K h}^{-1}$  for positive values,  $0.1 \text{ K h}^{-1}$  for negative). The radiative forcing field shown in Fig. 5a is the combination of LW and SW forcing, averaged through a diurnal cycle. The cloud-top cooling in the CRF-on TC is what remains after the counteracting processes of LW emission (Fig. 6a), which occurred throughout the day, and SW absorption (Fig. 6b), which was present for roughly half of the 24-h averaging period.

Next, we subdivide the radiative response averaged over a 350-km radius centered on the storm into three parts, each integrated over a full diurnal cycle (Fig. 7). First, there is the clear-sky forcing in a quiescent environment (Fig. 7a) without convection of any kind.<sup>2</sup> LW cooling of approximately  $2 \text{ K day}^{-1}$  occurred through much of the troposphere, along with  $<1 \text{ K day}^{-1}$  of solar heating, resulting in a net cooling of  $1\text{--}1.5 \text{ K day}^{-1}$ . Through convective activity, the temperature and water vapor fields become perturbed within the TC region, resulting in the somewhat altered tendency profiles seen in the RRTMG CRF-off case (Fig. 7b).

In contrast, the CRF-on profiles represent a dramatic shift from the undisturbed clear-sky forcing. The direct impact of the anvil is readily apparent: SW absorption of up to  $4 \text{ K day}^{-1}$  has occurred at 14 km with a reduction farther below, a likely consequence of anvil shading. The LW cooling at cloud top is even larger, almost  $-9 \text{ K day}^{-1}$ , resulting in a net forcing of  $-4.5 \text{ K day}^{-1}$  at that level over the diurnal cycle. As the competition between SW and LW only exists when the sun is above the horizon, there is a substantial diurnal cycle in the cloud-top CRF. Below the 11-km level, the effect of CRF is to decrease the LW cooling, resulting in small warming at some altitudes, particularly in the upper troposphere. If the forcing computation were limited to the cloudy area, excluding the clear eye and the environment radially beyond the anvil, the warming would be a bit more apparent, as has already been seen (in Figs. 5a,c).

Figure 12 in Gray and Jacobson (1977) presents vertical profiles of diurnally averaged net radiative forcing for clear and disturbed (cloudy) tropical regions. These strongly resemble our Figs. 7a and 7c, respectively, suggesting that they may be reasonable in structure and magnitude. Parallel simulations with ARW that included other radiation treatments (including the Fu-Liou-Gu scheme as well as an older version of RRTMG) generated

<sup>2</sup>This profile was obtained from the fourth day of a simulation with RRTMG in which the initial bubble was not inserted, and thus no convection ever formed.

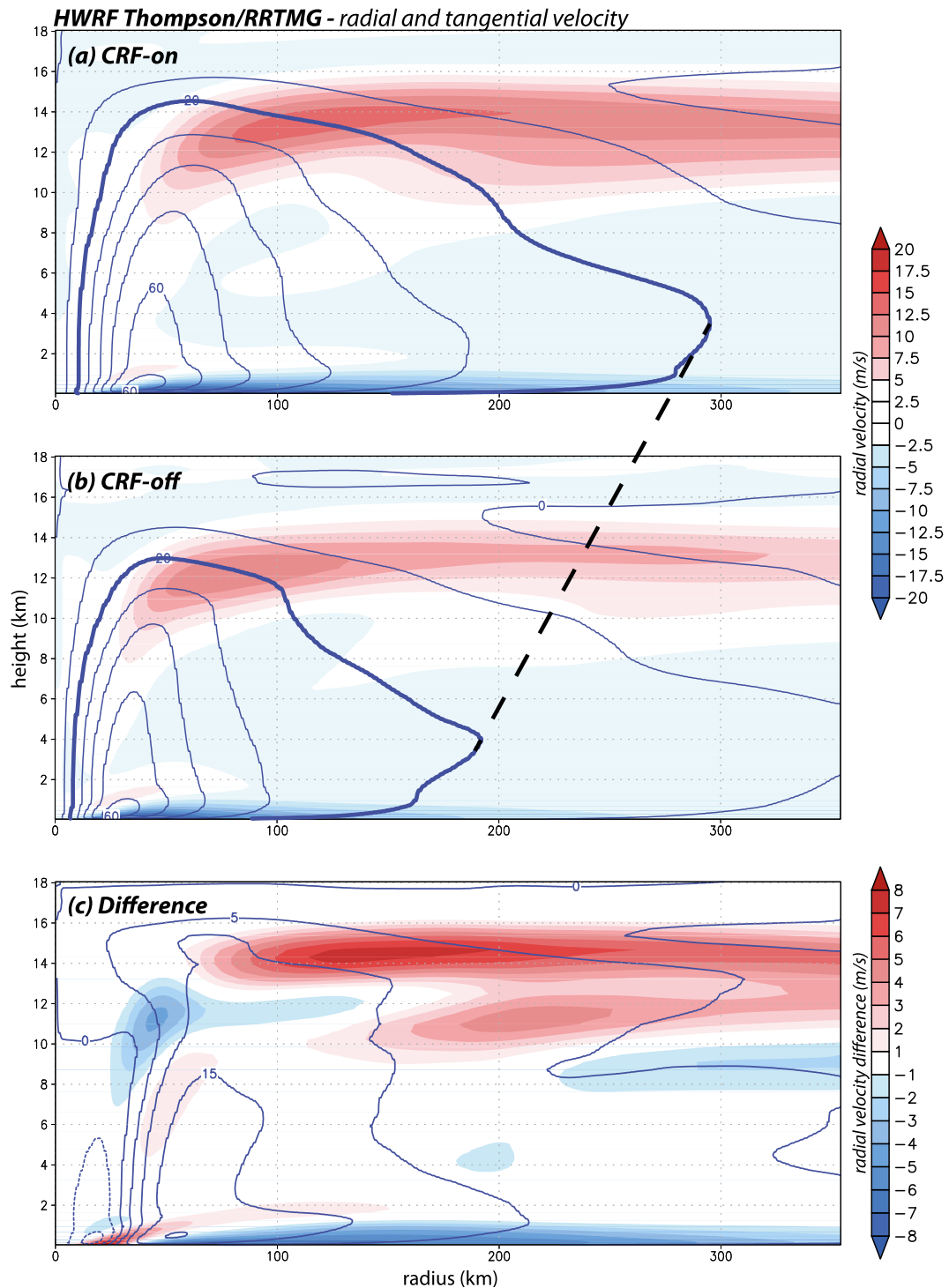


FIG. 4. Radius vs height cross sections showing the symmetric components of radial (shaded) and tangential (contoured at  $10 \text{ m s}^{-1}$ ) wind from HWRF simulations using Thompson MP and RRTMG radiation for the (a) CRF-on and (b) CRF-off cases. The  $20 \text{ m s}^{-1}$  tangential wind contour is highlighted. (c) The CRF-on minus CRF-off difference fields. Fields are computed from D2.

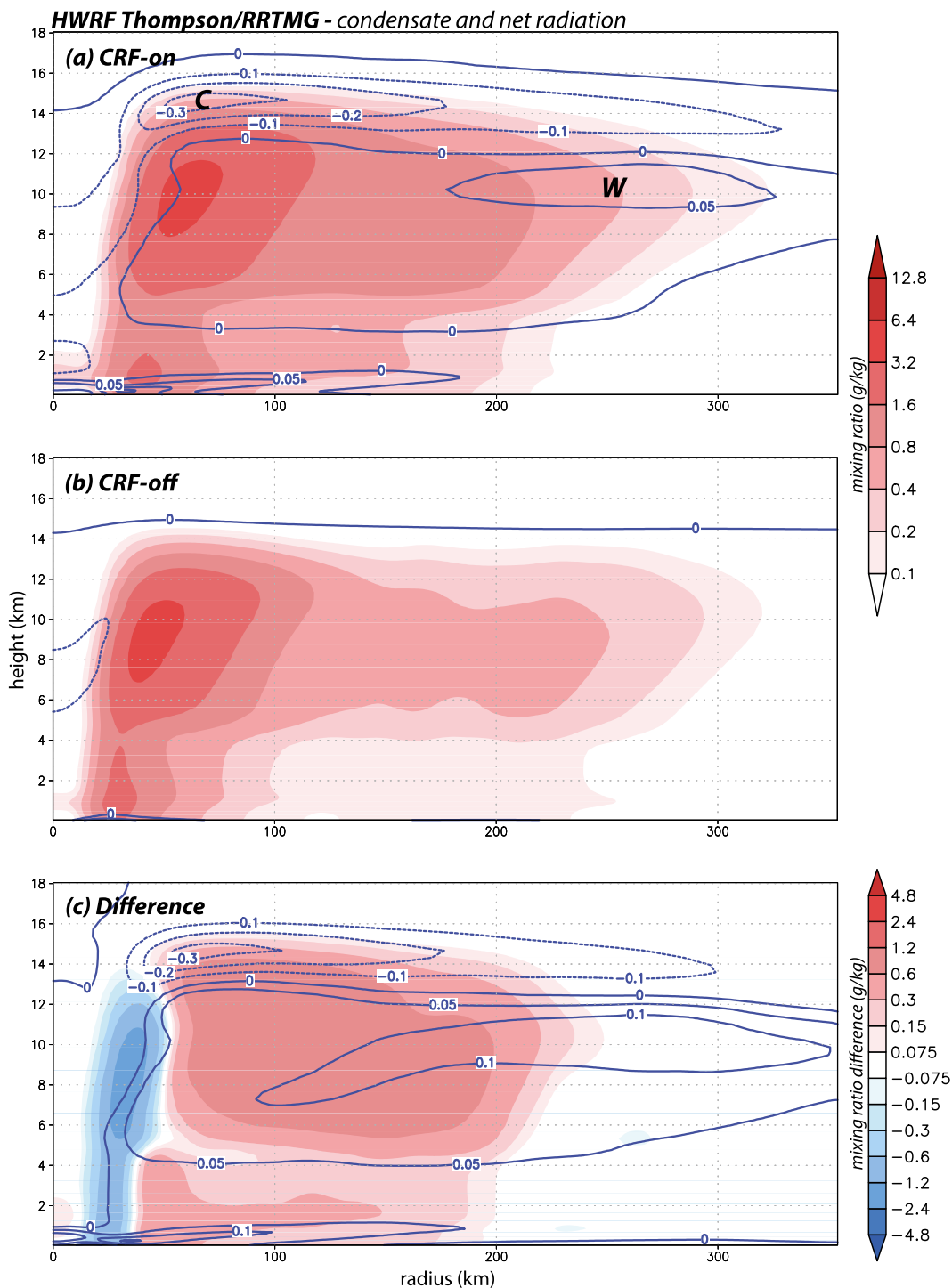


FIG. 5. As in Fig. 4, but for total condensate (shaded, note logarithmic scale) and net radiative forcing [negative (dashed) contour interval  $0.1 \text{ K h}^{-1}$ , and positive (solid) interval  $0.05 \text{ K h}^{-1}$ ] field. As defined in the text, “radiative forcing” refers to the potential temperature tendency owing to radiative processes. Letters “C” and “W” highlight local maxima of diabatic cooling and warming, respectively. Fields are computed from D2.

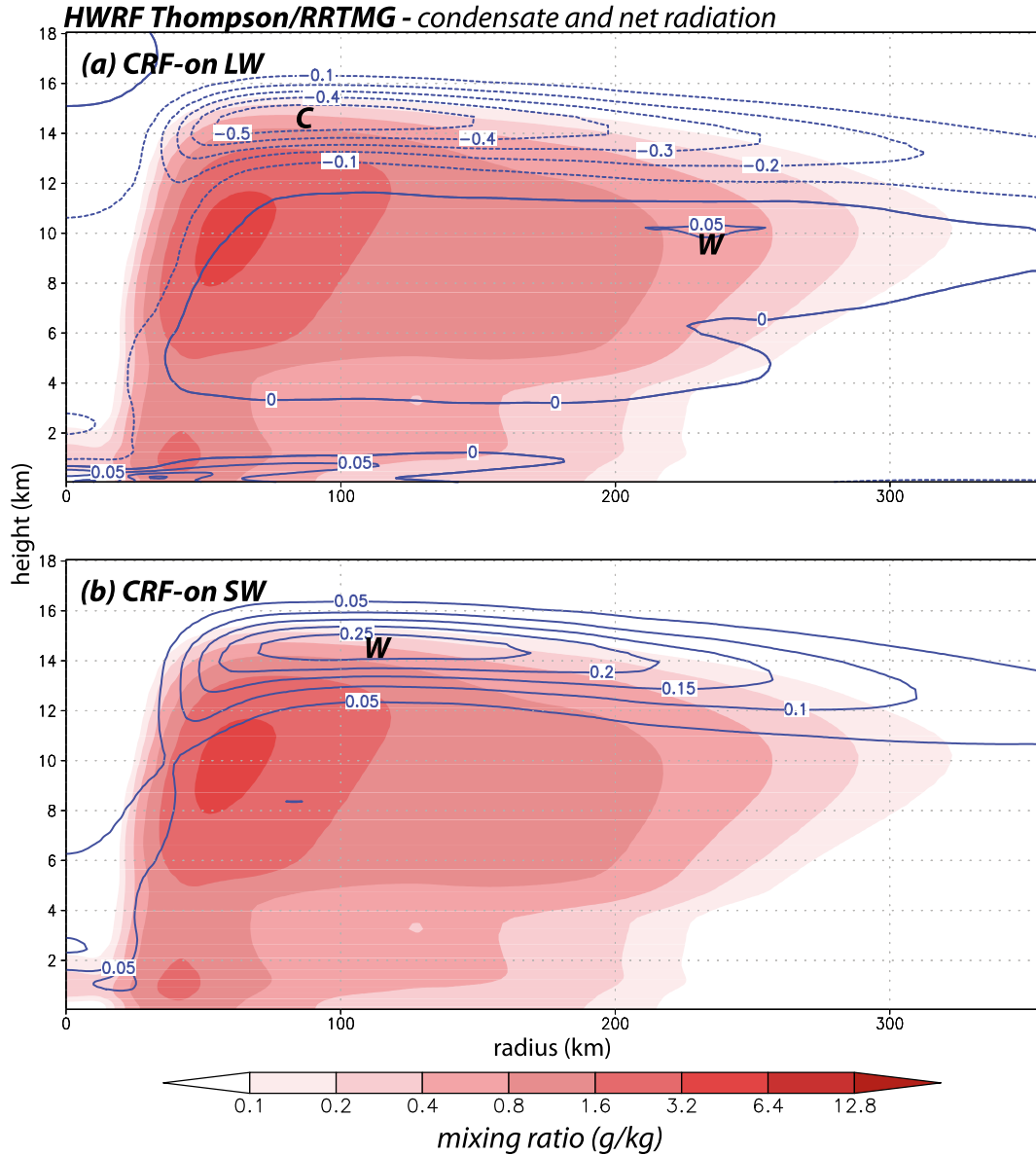


FIG. 6. The LW and SW contributions to the CRF-on storm net radiative forcing field, averaged over a full diurnal cycle, superposed on the total condensate field (cf. Fig. 5a).

comparable vertical profiles in the cloudy region (not shown), so the major difference is between transparent and nontransparent clouds rather than among the various schemes. The lone exception is the GFDL package that has been used operationally in HWRf since its inception. Compared to other radiation parameterizations, the GFDL scheme handles deep cloud layers in a different manner, one which effectively spreads the cloud-radiative forcing through the layer. This appears to explain why the GFDL scheme reveals little to no CRF (Fig. 7d). Its storm structures (not shown) are similar to the RRTMG CRF-off case.

Finally, the enhanced convective activity in the CRF-on storm is also apparent in the composite field of potential temperature tendency owing to latent heating and cooling (Fig. 8). This “microphysics forcing” is larger in two layers residing beyond the 60-km radial, again separated by the melting layer. The enhanced activity is likely responsible for the generally higher equivalent potential temperatures ( $\theta_e$ ) seen beyond the eyewall (Fig. 8). In the CRF-off case, low- $\theta_e$  air extends inward much closer to the eyewall, into which it might be ventilated, potentially reducing storm intensity (Tang and Emanuel 2012). The enhanced convective activity in

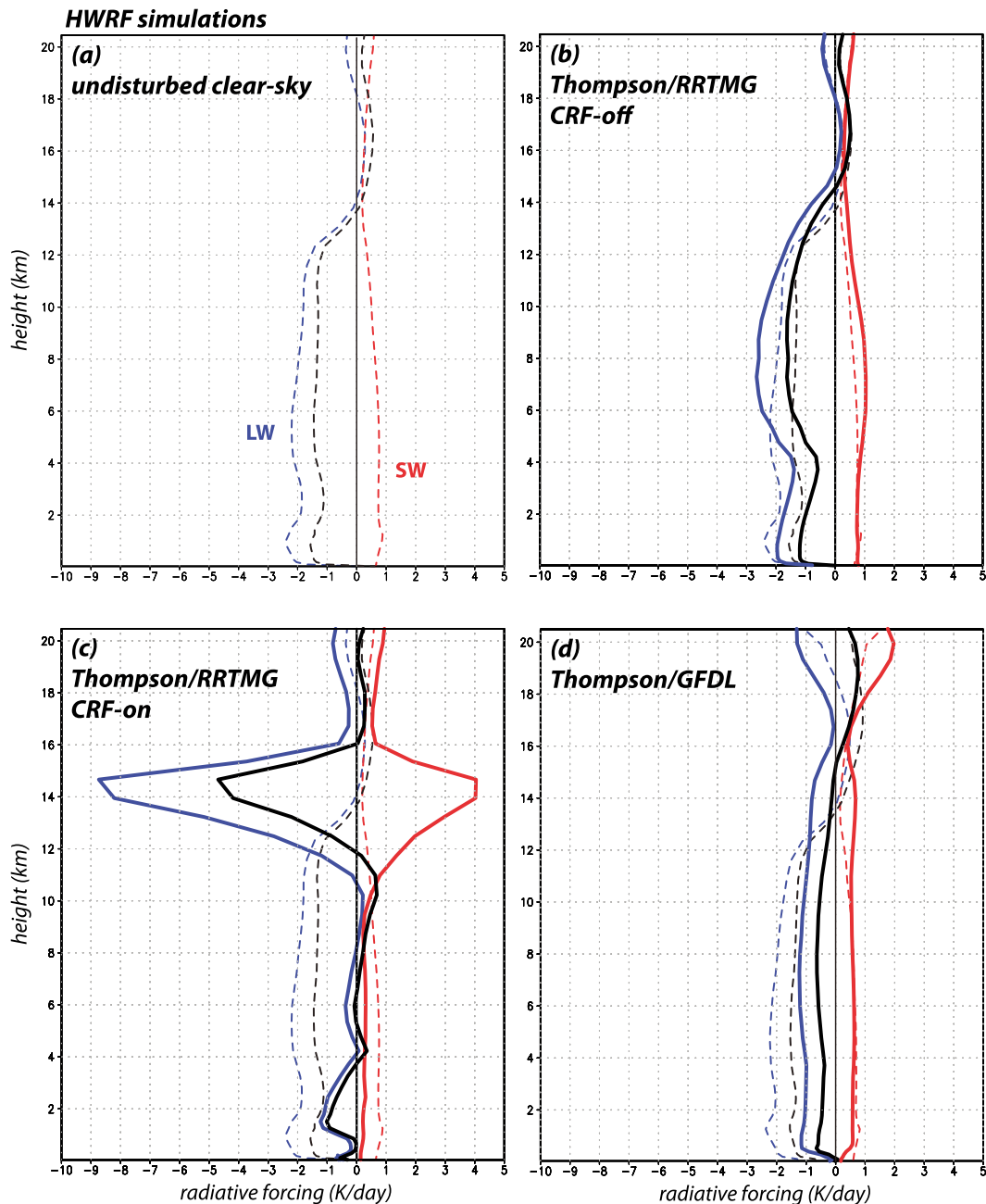


FIG. 7. Vertical profiles of areally and temporally averaged radiative forcing tendencies, showing LW (blue), SW (red), and net (black) radiation ( $\text{K day}^{-1}$ ). (a) The undisturbed clear-sky profile from the RRTMG scheme is also included for the Thompson (b) CRF-on and (c) CRF-off cases. (d) The Thompson/GFDL storm; its dashed lines represent the GFDL scheme's undisturbed clear-sky profiles.

the CRF-on storm might also lead to weaker TCs (e.g., Wang 2009; Bao et al. 2012) and/or secondary eyewall formation (e.g., Rozoff et al. 2012), although evidence is emerging that outer-core lightning activity may presage rapid intensification (DeMaria et al. 2012). Therefore, the net effect of CRF on intensity is unclear and likely complex, if not case dependent.

#### 4. The physics of CRF

Results in section 3 show that inclusion of cloud-radiative forcing in HWRF results in TCs that have wider eyes, broader tangential wind fields, and stronger upper-level outflow (as well as lower-tropospheric inflow). Comparable results were obtained in a parallel experiment

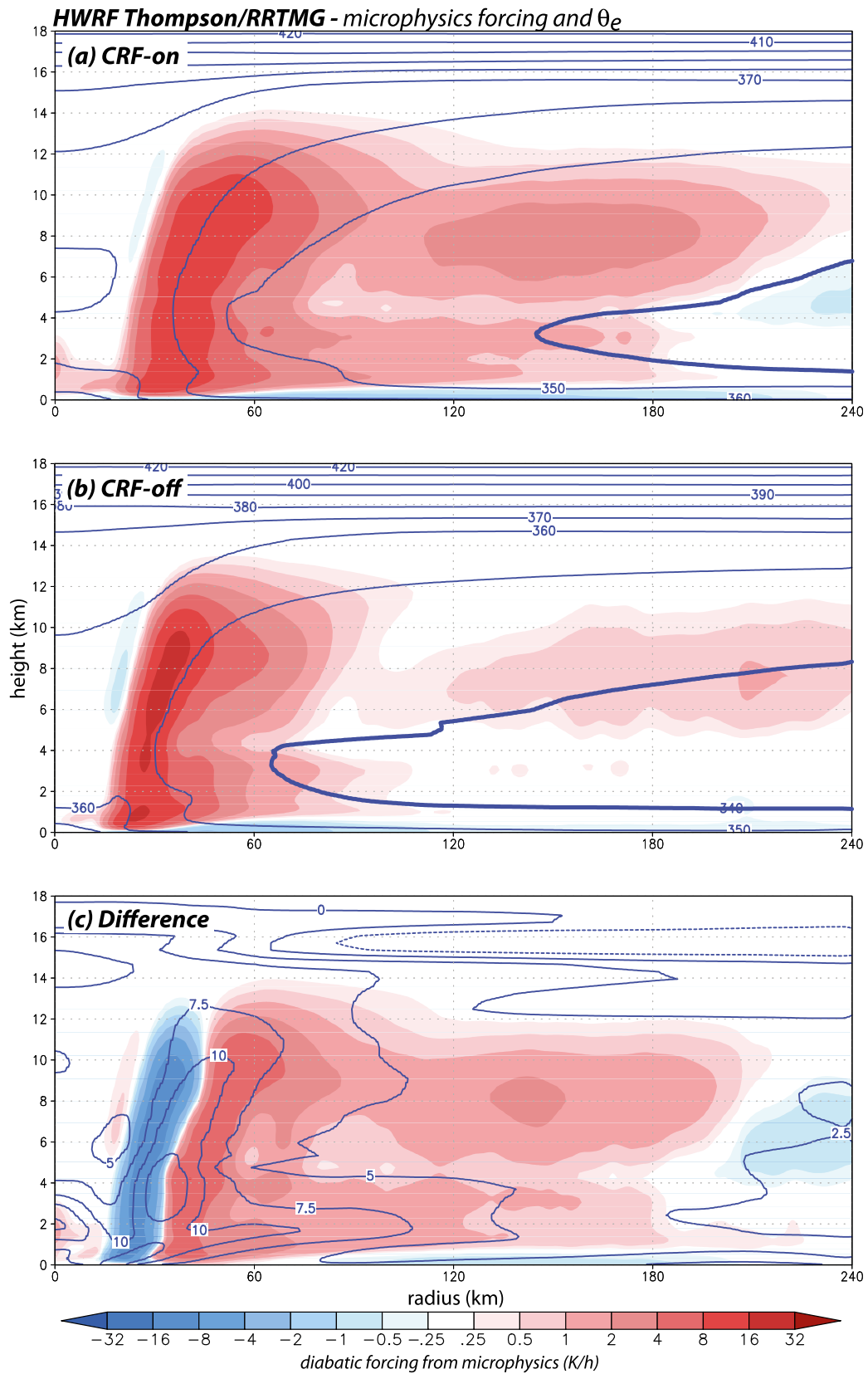
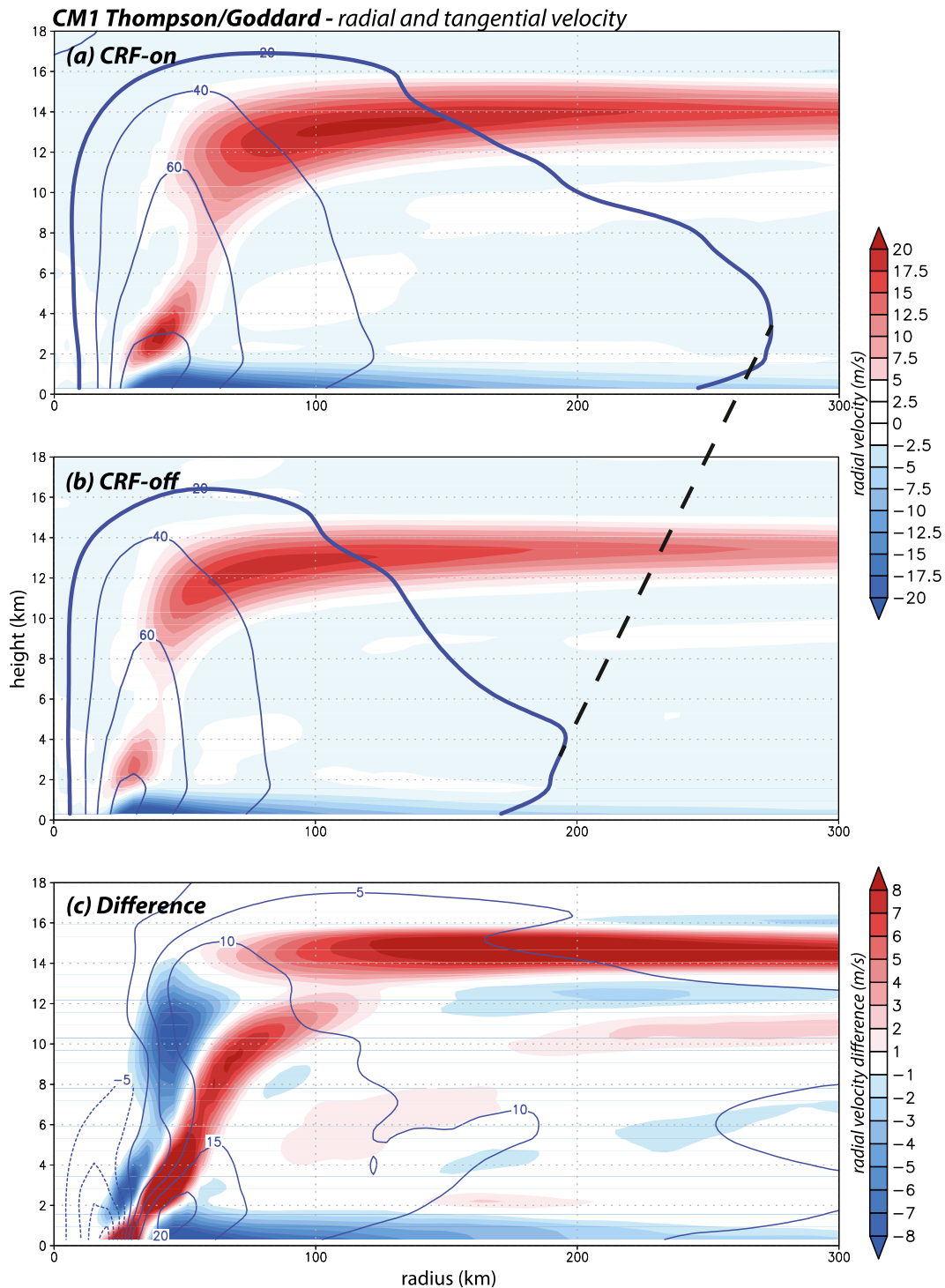


FIG. 8. As in Fig. 4, but for microphysics forcing (shaded, note logarithmic scale) and equivalent potential temperature (10-K contours, 340-K contour highlighted), computed from D3. As defined in the text, “microphysics forcing” refers to the potential temperature tendency owing to latent heating and cooling.



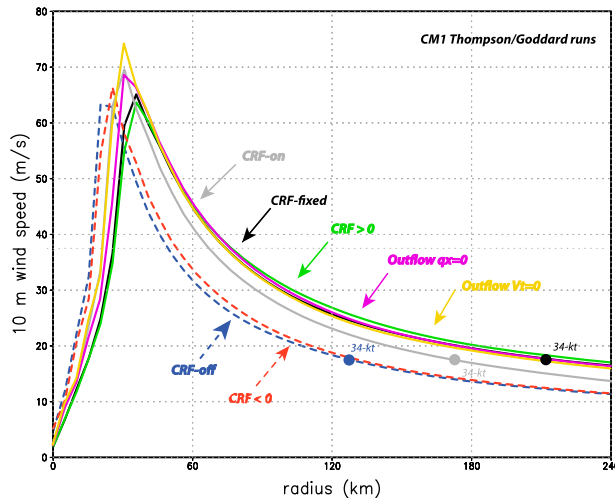


FIG. 10. Radial profiles of the temporally averaged 10-m wind speed from CM1 experiments using Thompson MP and Goddard radiation and including CRF-on, CRF-off and CRF-fixed cases. Simulations “CRF > 0” and “CRF < 0” are versions of CRF-fixed in which only the positive and negative CRF forcings were retained. Experiments “Outflow  $V_t = 0$ ” and “Outflow  $q_x = 0$ ” are versions of CRF fixed in which the terminal velocity and mixing ratio of hydrometeors in the outflow were zeroed, respectively. See text for more information. Radii of the 34-kt ( $17.5 \text{ m s}^{-1}$ ) wind are indicated.

using a semi-idealized version of ARW (not shown), which permitted examination of a wider variety of radiation and microphysics schemes. In this section, we employ the far more easily manipulated CM1 model in axisymmetric mode to explore how and why CRF has these impacts, and conclude with a revisit of HWRF.

#### a. Initial CM1 experiments with moisture

The structural response to the inclusion of cloud-radiative forcing is qualitatively similar between the CM1 and HWRF experiments, despite differences with respect to the dynamical framework, initialization, and model physics. Again, the CRF-on version possesses a stronger secondary circulation, a wider eye, and a broader tangential wind field (Fig. 9), including a notably larger radius for the 34-kt near-surface wind (Fig. 10). Its condensate field is again wider, indicative of enhanced convective activity beyond the inner core, and the radiative forcing field is comparable in magnitude and spatial pattern, despite the employment of a different radiation parameterization (Figs. 11a–c). That said, the LW warming within the cloud is somewhat larger in the present CRF-on example, a consequence of the fact that the axisymmetric storm, by definition, has no azimuthal asymmetries. Similarly enhanced warming was seen in  $f$ -plane versions of our HWRF and ARW experiments (not shown), which generate very symmetric TC structures.

The cloud-radiative forcing encompasses the radial extent of the cloudy area, which progresses outward as the storm evolves and matures. However, this does not necessarily mean that the relatively small forcing associated with the CRF actively participated in the anvil expansion. That linkage is tested in an experiment dubbed CRF-fixed. The radiation scheme computes both total and clear-sky radiative tendencies, with the CRF being the difference between the two. In the CRF-fixed run, CRF was deactivated and the temporally averaged cloud-radiative forcing field from the CRF-on experiment (seen in Fig. 11a) was externally imposed and held fixed from the initialization time, making the influence of clouds on radiation independent of the convective activity, and where and when clouds happen to form. This removes not only most of the diurnal cycle in the radiative forcing, but also the gestational period during which the anvil develops.<sup>3</sup>

The result of external imposition of the cloud-radiative forcing is the development of a model TC (Fig. 11d) with an anvil extent that resembles the CRF-on storm (Fig. 11a) far more closely than it does the original CRF-off case (Fig. 11b). Its secondary circulation (Fig. 12a) and eye width are comparable to those of the CRF-on TC, as emphasized by the difference field with respect to the simulation with transparent clouds (cf. Fig. 12d with Fig. 9c). Its tangential wind field is even broader than in the CRF-on case (see also Fig. 10), a consequence of having a mature radiative forcing field from the start. After all, the outer tangential wind field tends to continue expanding with time (not shown), something observed in tropical cyclones as well (cf. Weatherford and Gray 1988a,b).

The next experiment tests the relative contribution of the imposed radiative forcing’s cooling (mainly at cloud top) and warming (largely confined to the cloudy area) on the storm structure. For the “CRF < 0” simulation (Fig. 11e), we retained the cloud-radiative component from the CRF-fixed simulation solely where it resulted in cooling. Similarly, the CRF > 0 run (Fig. 11f) was created by keeping the cloud-radiative forcing only where it was positive. For convenience, these simulations were based on the CRF-fixed setup and, again, the clear-sky forcing was permitted to vary. Fixing the net radiation instead had only a minor impact on the results and none on the conclusions. Similarly, simulations in which the total radiation was permitted to vary, but with

<sup>3</sup> A simulation in which the total radiation, including the clear-sky component, was fixed showed very little difference from the CRF-fixed run. That run did result in complete removal of the radiation diurnal cycle.

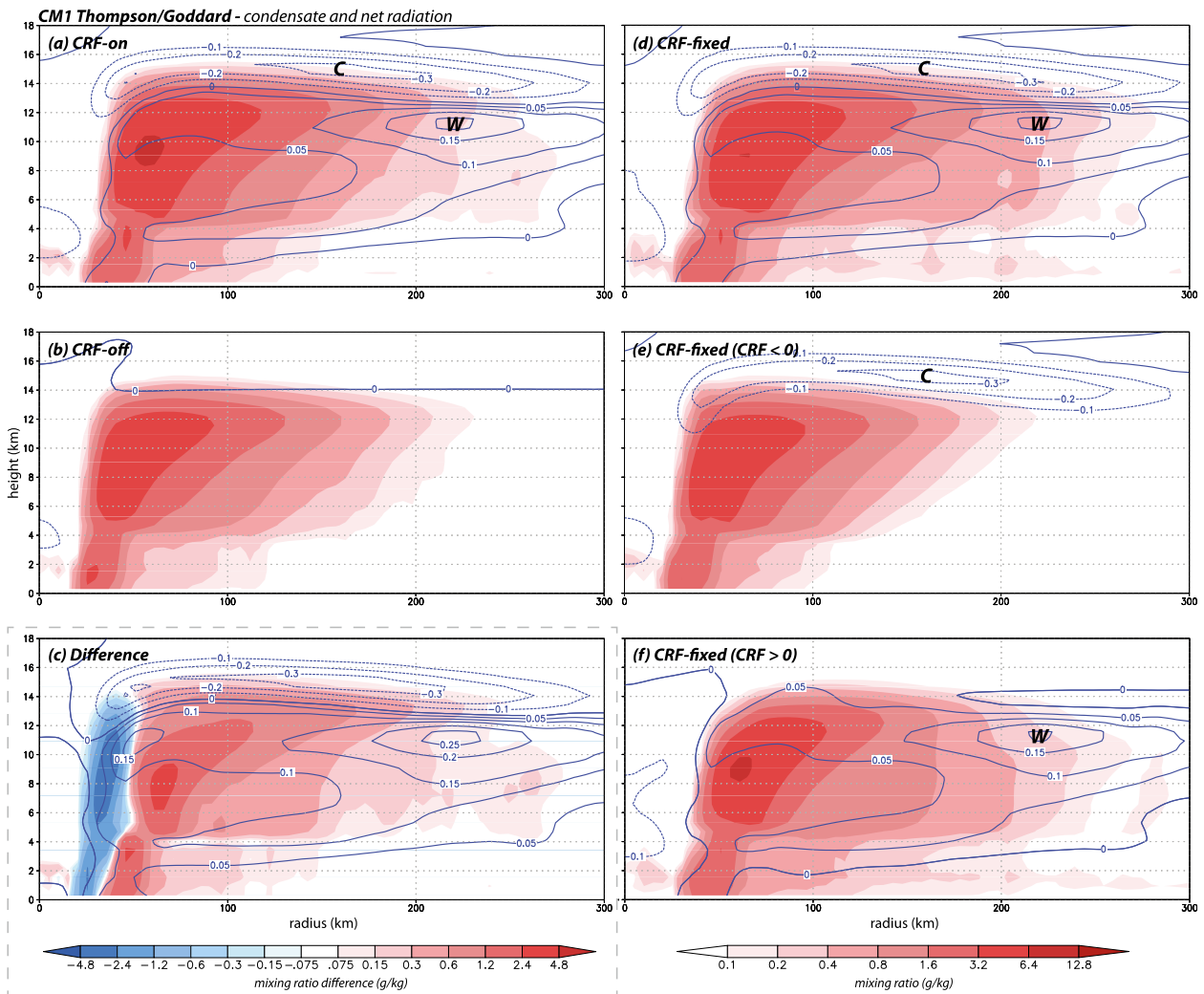


FIG. 11. Total condensate (shaded, note logarithmic scale) and net radiation [negative (dashed) contour interval  $0.1 \text{ K h}^{-1}$ , and positive (solid) interval  $0.05 \text{ K h}^{-1}$ ] for CM1 Thompson/Goddard model storms, averaged as in Fig. 9: (a) CRF-on, (b) CRF-off, and (c) difference between CRF-on and CRF-off. At right, results from members of the CRF-fixed experiment: (d) CRF-fixed, (e) CRF-fixed with only negative CRF forcing ( $\text{CRF} < 0$ ), and (f) CRF-fixed with only positive CRF forcing ( $\text{CRF} > 0$ ). Letters “C” and “W” highlight local maxima of diabatic cooling and warming, respectively. In (c), the color legend at bottom left is used, other panels use the bottom-right legend.

only the positive or negative forcings retained, yielded similar results and identical conclusions.<sup>4</sup>

Although the cloud-top cooling is larger in magnitude, the  $\text{CRF} < 0$  run shows that it has very little influence on either anvil width (Fig. 11e) or the tangential and radial wind fields (Figs. 10 and 12b,e), all being far more comparable to the CRF-off storm than to its CRF-on counterpart. The only material difference appears to be in eye size, which is slightly larger than in the original CRF-off storm (Fig. 12b). In pointed contrast, the

$\text{CRF} > 0$  TC (Figs. 10, 11f, and 12c,f) strongly resembles the CRF-fixed storm in all important aspects, explaining most of the eye width shift and essentially all of the wind field intensification and anvil expansion, despite being much smaller in magnitude than the cloud-top cooling. Thus, it is the weak within-cloud warming, a consequence of the influence of hydrometeors on LW absorption and emission, that is relevant to the storm expansion.

#### b. Further experiments with dry and moist models

We hypothesize that the within-cloud forcing has both direct and indirect effects and explore the former with a dry version of the CM1 axisymmetric model, in a complementary effort to more simplified and theoretical treatments

<sup>4</sup>This strategy is pursued in the HWRF version of this experiment, presented in section 4c.

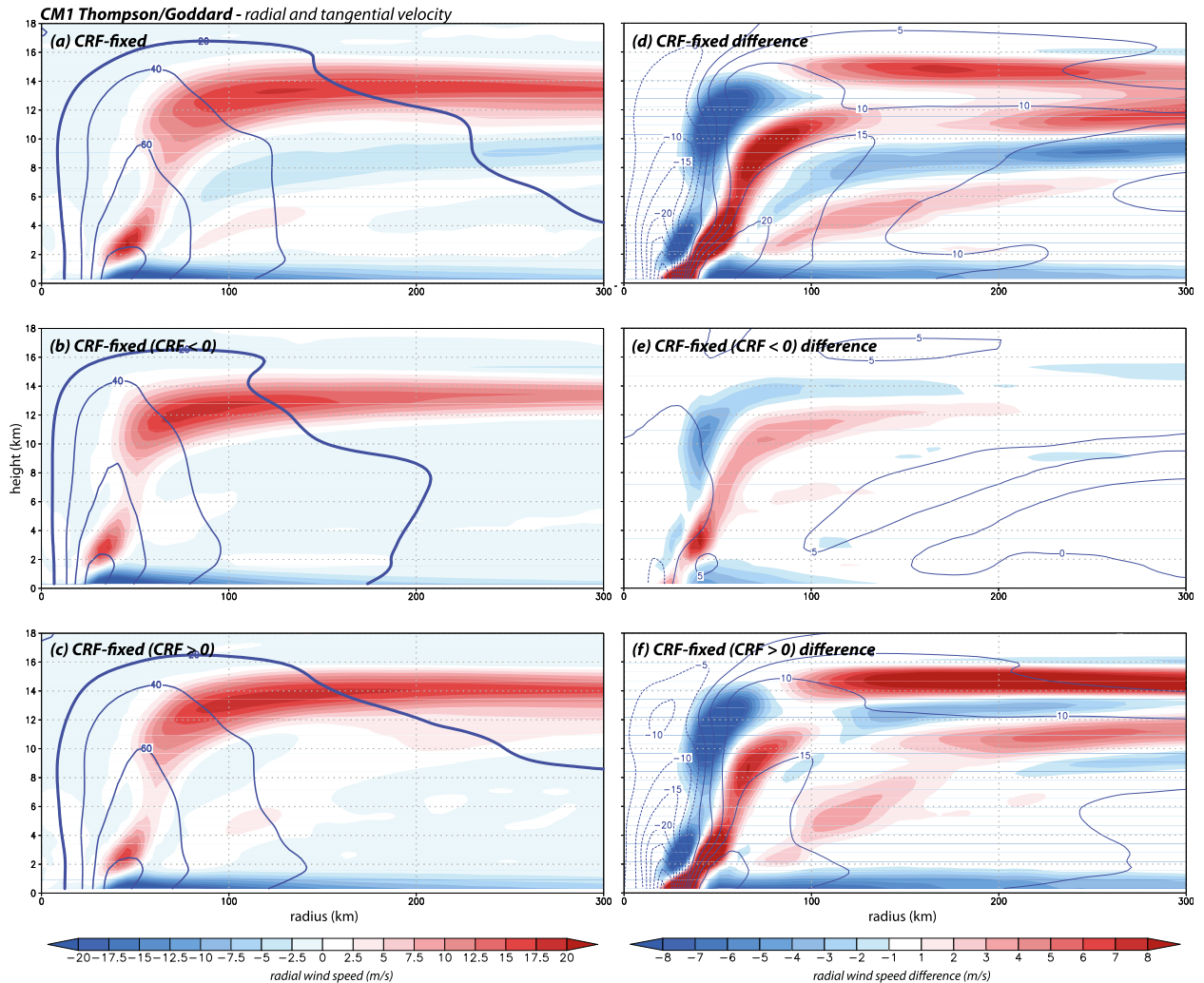


FIG. 12. As in Fig. 9, but for members of the CM1 CRF-fixed experiment. Averaged fields for (a) CRF-fixed, (b) CRF-fixed with only negative CRF forcing ( $CRF < 0$ ), and (c) CRF-fixed with only positive CRF forcing ( $CRF > 0$ ). Difference fields with respect to CRF-off case for (d) CRF-fixed, (e) only negative CRF forcing ( $CRF < 0$ ), and (f) only positive CRF forcing ( $CRF > 0$ ).

of heat and momentum sources (e.g., Willoughby 1979; Shapiro and Willoughby 1982; Schubert and Hack 1982; Holland and Merrill 1984). Moisture, the surface latent heat flux, and the initial vortex were removed for these simulations, which were otherwise configured identically to the runs described above. At each time step, the model was provided with the difference between the CRF-on storm's temporally averaged cloudy and clear-sky radiative tendencies, resulting in a forcing field that is only subtly different from that used in the moist CRF-fixed experiments (cf. Figs. 11d and 13a) since, again, the CRF dominated the net radiation.<sup>5</sup> The  $CRF < 0$  and

$CRF > 0$  simulations reveal the relative influences of the cloud-top cooling and in-cloud warming.

With respect to radial velocity, the dry model shows that the CRF diabatic forcing generates gentle but significant radial outflow in the upper troposphere, sandwiched between the cooling and the warming (Fig. 13a). This field develops very rapidly in response to the imposed forcing, in a matter of a few hours (not shown). It is again seen that most of this outflow response is generated by the positive radiative forcing that occupies much of the troposphere, and not the cooling at cloud top (Figs. 13b,c). In any event, that enhanced outflow transports radially outward the same hydrometeors that are responsible for causing the CRF in the first place. Thus, there is a potential *positive feedback* between the cloud-radiative forcing and the outflow enhancement that

<sup>5</sup> Dry simulations using the net radiation forcing field shown in Fig. 11d were nearly indistinguishable from those shown in this subsection.

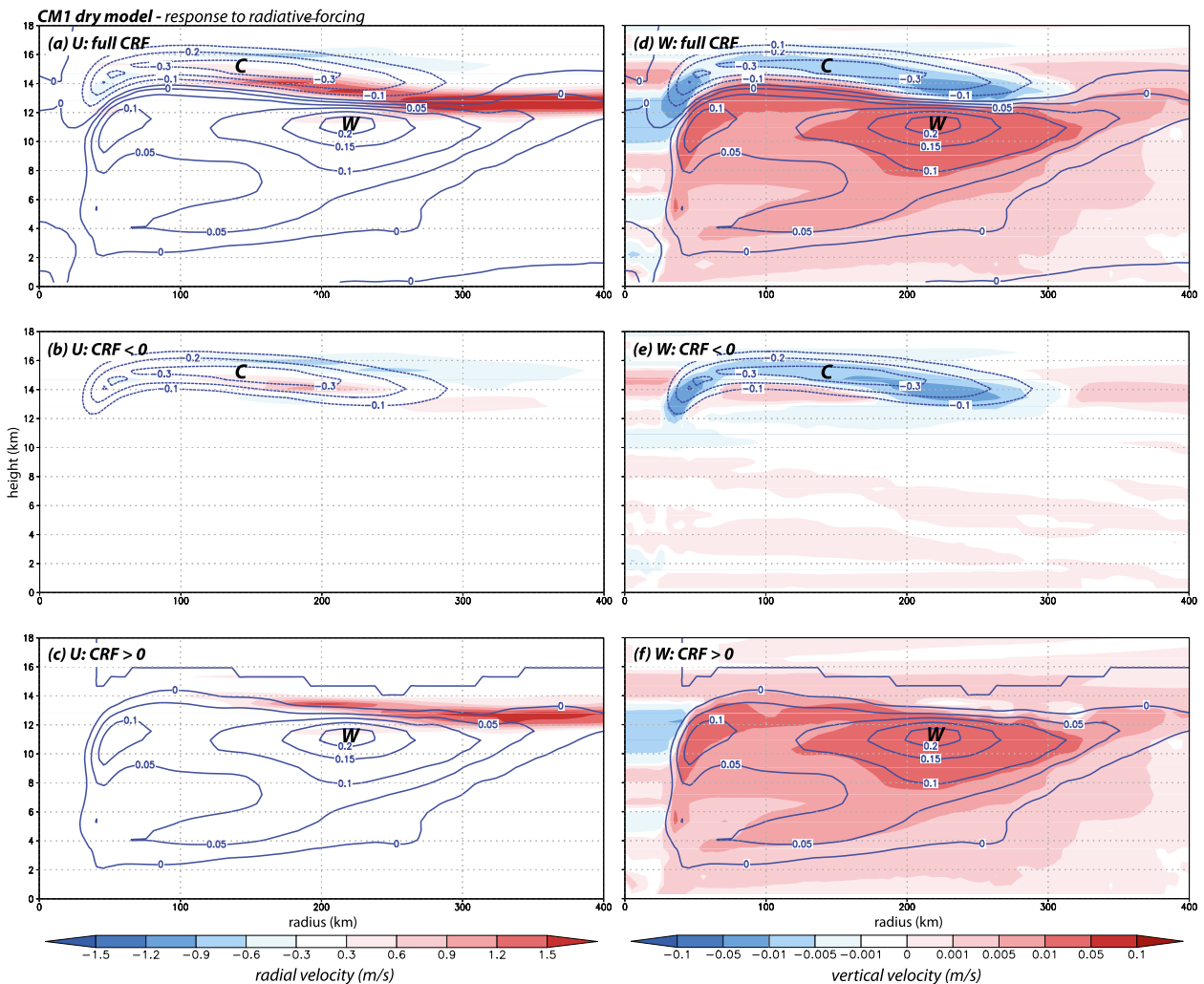


FIG. 13. Simulations from the dry version of CM1, forced by the difference between the CRF-on storm cloud and clear-sky radiative tendencies (contoured as in Fig. 11a), averaged from day 9 to 12. Radial velocity response (shaded) for the (a) full CRF forcing field, (b) CRF < 0 component, and (c) CRF > 0 component. Vertical velocity response (shaded) for the (d) full CRF forcing field, (e) CRF < 0 component, and (f) CRF > 0 component. Dry fields are averaged over the simulations' first 4 days.

results in farther outward expansion of both the cloudy area and the radial outflow. Further, owing to the competition between LW and SW radiation that reduces the net cloud-top cooling during daylight hours, this feedback may make an important contribution to the diurnal pulsing in the IR cloud field recently noted by J. Dunion (2013, personal communication) and colleagues.

That positive feedback, however, is not sufficient by itself to explain the more radially extensive deep convective activity that occurs when cloud-radiative forcings are included. This is demonstrated using experiments based on the CRF-fixed case for clarity and simplicity, as altering hydrometeor contents and distributions would otherwise modify the cloud-radiative forcing. It was surmised that the settling of hydrometeors from the

CRF-enhanced radial outflow might progressively moisten the outer-core region, eventually making it more supportive of deep convection. Yet, preventing outward-advected hydrometeors from settling out of the upper-tropospheric outflow (by assigning them zero terminal velocity,  $V_t$ ) did not reduce either convective activity in the outer core (not shown) or the width of the tangential wind field relative to the CRF-fixed storm, characteristics that will soon be shown to be linked. Indeed, its near-surface wind profile and 34-kt wind radius were nearly identical to the CRF-fixed case on which it was based (see “Outflow  $V_t = 0$ ” in Fig. 10).

Furthermore, even complete *removal* of the hydrometeors within the radial outflow, once they passed beyond the radius of 100 km (about 2–3 times the radius

of maximum wind), had little impact on the convective activity (not shown) or the tangential wind field, as its near-surface wind profile was again nearly identical to that of the CRF-fixed storm (see “Outflow  $q_x = 0$ ” in Fig. 10). From these experiments, it is determined that the enhanced convective activity is not a consequence of hydrometeor seeding or moistening associated with the CRF-enhanced outflow. We note that these results are broadly compatible with, and further extend, the hydrometeor fall speed experiments reported in Fovell et al. (2009).

Therefore, we believe the most effective direct impact of the cloud–radiative forcing lies not in the enhanced upper-tropospheric outflow but, instead, in the *vertical circulation* it induces (Figs. 13d–f). The deep in-cloud warming (Fig. 13f), in particular, provokes ascent through much of the troposphere that is gentle in magnitude but potentially significant because of its spatial extent and temporal persistence. Upward motions of about  $0.0075 \text{ m s}^{-1}$ , seen in the midtroposphere around 150 km from the eye, may seem negligible at first but can result in over 600 m of ascent over the course of a day, increasing the relative humidity through a wide and deep area. As it is entirely missing when clouds are treated as transparent, this ascent directly instigates, as well as supports, the enhanced convective activity beyond the inner core in the moist CRF-active simulations. In other words, the cloud–radiative forcing produces ascent throughout an extended region, one that leads to enhanced convective activity throughout the outer core.

The final link is to relate the radially expanded diabatic heating that results from increased convection to the broader wind field also seen in every CRF-active simulation, which can be anticipated from prior work using Sawyer–Eliassen models (e.g., Hack and Schubert 1986). As in the fully three-dimensional HWRF simulations, the CRF-on axisymmetric storm possessed a more radially extensive heating field associated with microphysics (Fig. 14a). A portion of this forcing field, restricted to positive values beyond 100-km radius, was inserted into the dry model (Figs. 14b,c). The responses suggest that the augmented outer-region heating associated with cloud–radiative forcing can broaden the cyclonic wind field in the lower troposphere as well as augment the secondary circulation (including the upper-level outflow). This is generally consistent with the findings of Fovell et al. (2009), Hill and Lackmann (2009), Wang (2009), and Xu and Wang (2010a,b), among others.

### c. Confirmation in HWRF

We now confirm that the sensitivity to the within-cloud LW warming that emerged from the axisymmetric

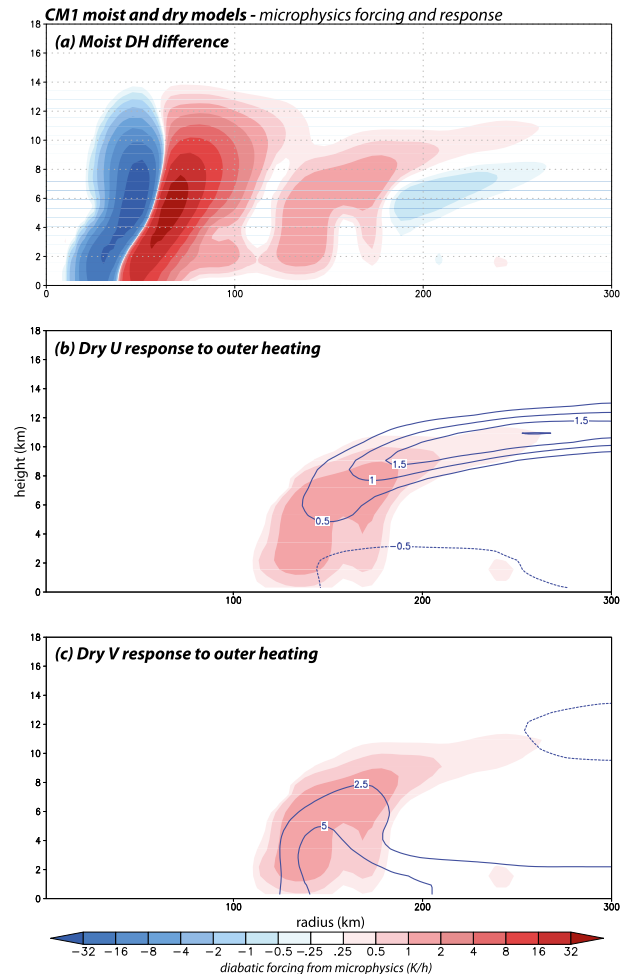


FIG. 14. (a) Temporally averaged net microphysics forcing difference field between the CM1 CRF-on and CRF-off storms, with the dry model response for (b) radial ( $0.5 \text{ m s}^{-1}$  contours) and (c) tangential velocity ( $2.5 \text{ m s}^{-1}$  contours), to the forcing field extracted from the moist model’s outer-core region. Input for the dry model was created by averaging positive forcings only. Dry model responses are averaged over the first 4 days.

simulations also occurs in the fully three-dimensional model, with HWRF versions of the CRF  $< 0$  and CRF  $> 0$  experiments. For simplicity, the cloud–radiative forcing was permitted to vary in time and space in these runs, with either the negative or positive contributions of this forcing retained, respectively. As anticipated, the positive component of CRF suffices to broaden the cyclonic wind field near (Fig. 15) and above the surface (Fig. 16) while the cloud-top cooling has very little effect. With respect to eye width, secondary circulation strength, and the spatial coverage of convection (Fig. 17), the CRF  $> 0$  TC was nearly indistinguishable from its CRF-on counterpart (cf. Figs. 2 and 4).

In closing, we note that the CRF-active HWRF simulations evince some radiative heating in a shallow layer

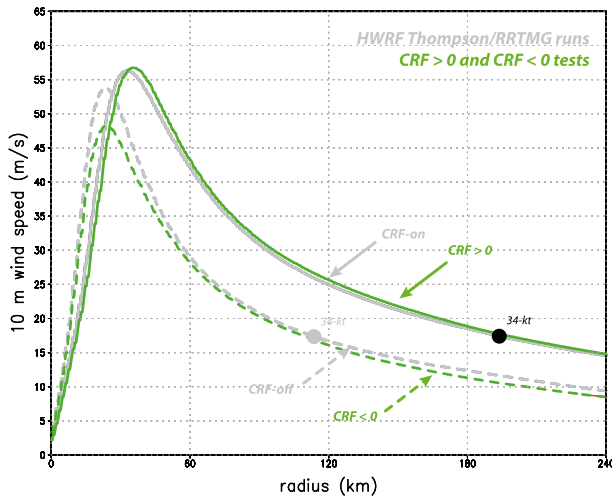


FIG. 15. As in Fig. 3, but emphasizing the HWRP Thompson/RRTMG CRF  $> 0$  and CRF  $< 0$  tests.

near the surface, within 200 km of the TC center (see Figs. 5a,c). Removing this had virtually no impact on the simulations (not shown).

## 5. Summary

Semi-idealized integrations of a preimplementation version of the Hurricane WRF model (HWRP) demonstrate how, and why, cloud-radiative forcing significantly modulates the structure and intensity of simulated tropical cyclone vortices. The version of the model that we used fully couples the Thompson microphysical parameterization (MP) to the RRTMG radiation scheme, allowing the MP to pass particle size and mass information to the radiation scheme, permitting the hydrometeors to more consistently modulate longwave and shortwave radiative tendencies. This modulation is primarily seen in the upper troposphere, above and within the hurricane's central dense overcast, with pronounced LW cooling along the anvil top and weak LW warming within the cirrus canopy, which reverses the large LW cooling that occurs in the troposphere under clear-sky conditions.

In response to this realistic radiative forcing, simulated storms with CRF active have a larger amount of convection and diabatic heating outside the eyewall, as well as faster outer-core winds as compared to simulated storms with CRF turned off. CRF-on storms also possess a stronger secondary circulation with faster radial inflow at the lowest levels and stronger outflow aloft with a thicker and more radially extensive anvil.

Simulations conducted with a simplified, axisymmetric cloud model confirm our HWRP results as well as

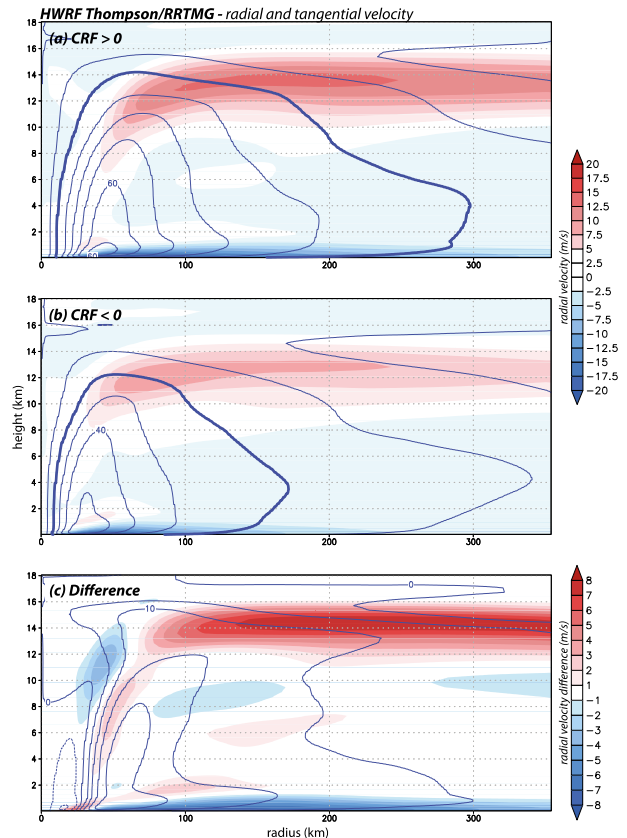


FIG. 16. As in Fig. 4, but for the HWRP versions of the (a) CRF  $> 0$  and (b) CRF  $< 0$  storms, and (c) the difference field between the two.

clearly show that the weak LW warming within the anvil is the most significant component of CRF. It is the portion of the CRF that directly encourages stronger upper-tropospheric radial outflow as well as slow, yet sustained, ascent throughout the outer core. This gentle ascent moistens the region outside the eyewall, enhancing convective activity, elevating the equivalent potential temperature, and increasing the size of the TC—consistent with the results of other high-resolution hurricane simulations (Hill and Lackmann 2009; Wang 2009; Xu and Wang 2010a; Fudeyasu and Wang 2011).

In this study, CRF had only a minor and inconsistent impact on the maximum tangential wind. However, it is very clear that the combined direct and indirect impact of CRF is to foster a broader storm circulation possessing a larger eye and an outward-shifted radius of maximum winds, all other factors being equal. Note in particular that the radial extent of the 34-kt wind in the HWRP CRF-on storm was significantly larger, by over 70%. As a consequence, accurate treatment of cloud-radiative forcing may be important operationally, as the radial extent on the wind field is a crucial

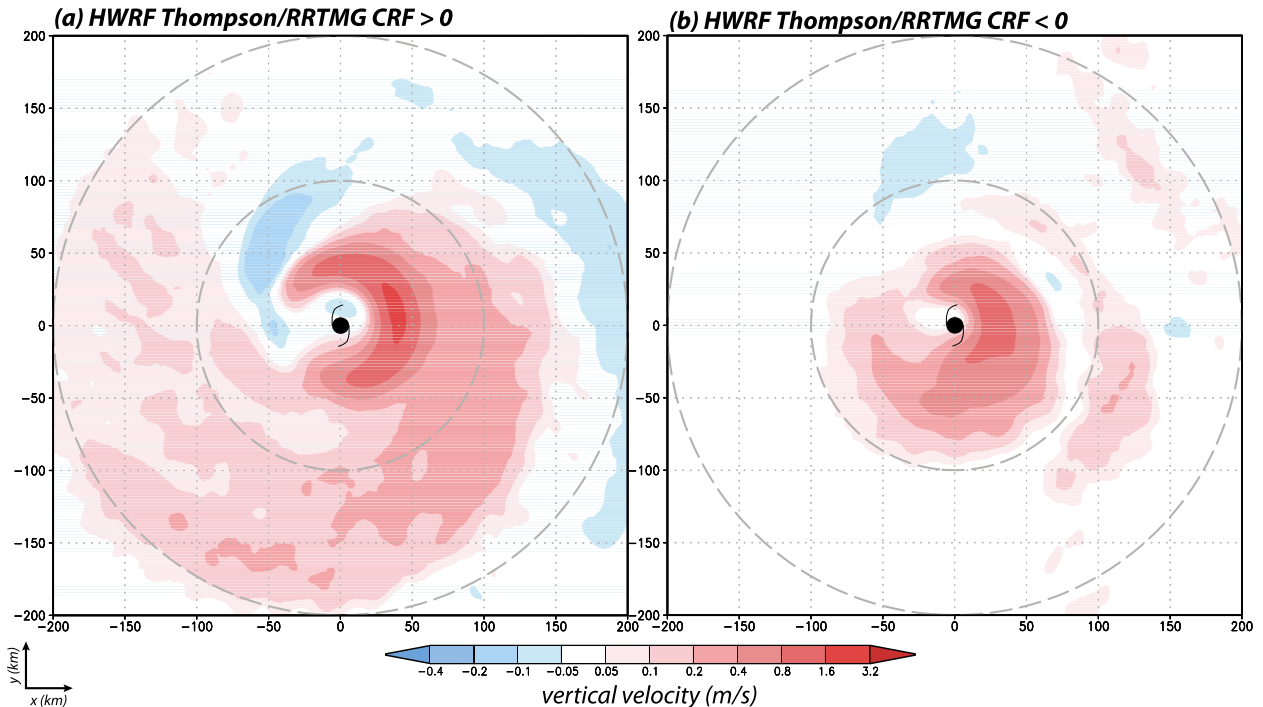


FIG. 17. As in Fig. 2, but for the HWRP versions of the (a) CRF > 0 and (b) CRF < 0 storms.

component of storm-surge forecasting (e.g., Lin and Chavas 2012).

Finally, it is worth noting that the GFDL radiation package, which has been used operationally in HWRP since its inception, handles deep cloud layers in a completely different manner than RRTMG. This scheme essentially spreads the cloud radiative forcing throughout a deep layer and produces simulated hurricane structures similar to our RRTMG CRF-off case. If, as anticipated, the Thompson-RRTMG suite is activated within the operational HWRP in 2014, we expect significant testing and validation will be needed to evaluate the reality of the broader and more convectively active storms that could result from model physics that produces deep clouds that are considerably less transparent to radiation.

*Acknowledgments.* The authors gratefully acknowledge the assistance of Drs. Ligia Bernardet, Mrinal Biswas, Gregory Thompson, and Brad Ferrier. Thanks also to Dr. George Bryan for use of his CM1 cloud model. The efforts of the editor and three anonymous referees are appreciated. This work was supported by the National Atmospheric and Oceanic Administration's Hurricane Forecast Improvement Program (HFIP) under Grant NA12NWS4680009 and by the National Aeronautics and Space Administration's Hurricane Science Research Program under Grant NNX12AJ83G.

## REFERENCES

- Bao, J.-W., S. G. Gopalakrishnan, S. A. Michelson, F. D. Marks, and M. T. Montgomery, 2012: Impact of physics representations in the HWRFX on simulated hurricane structure and pressure-wind relationships. *Mon. Wea. Rev.*, **140**, 3278–3299.
- Bender, M., 1997: The effect of relative flow on the asymmetric structure in the interior of hurricanes. *J. Atmos. Sci.*, **54**, 703–724.
- Braun, S. A., and W.-K. Tao, 2000: Sensitivity of high-resolution simulations of Hurricane Bob (1991) to planetary boundary layer parameterizations. *Mon. Wea. Rev.*, **128**, 3941–3961.
- Bryan, G. H., and M. Fritsch, 2002: A benchmark simulation for moist nonhydrostatic numerical models. *Mon. Wea. Rev.*, **130**, 2917–2928.
- , and R. Rotunno, 2009: The maximum intensity of tropical cyclones in axisymmetric numerical model simulations. *Mon. Wea. Rev.*, **137**, 1770–1789.
- Cao, Y., R. G. Fovell, and K. L. Corbosiero, 2011: Tropical cyclone track and structure sensitivity to initialization in idealized simulations: A preliminary study. *Terr. Atmos. Oceanic Sci.*, **22** (6), 559–578.
- Chou, M. D., and M. J. Suarez, 1994: An efficient thermal infrared radiation parameterization for use in general circulation models. NASA Tech. Memo. 104606, 85 pp.
- Corbosiero, K. L., and J. Molinari, 2002: The effects of vertical wind shear on the distribution of convection in tropical cyclones. *Mon. Wea. Rev.*, **130**, 2110–2123.
- DeMaria, M., R. T. DeMaria, J. A. Knaff, and D. Molnar, 2012: Tropical cyclone lightning and rapid intensity change. *Mon. Wea. Rev.*, **140**, 1828–1842.
- Dudhia, J., 1989: Numerical study of convection observed during the winter monsoon experiment using a mesoscale two-dimensional model. *J. Atmos. Sci.*, **46**, 3077–3107.

- Ferrier, B. S., Y. Jin, T. Black, E. Rogers, and G. DiMego, 2002: Implementation of a new grid-scale cloud and precipitation scheme in NCEP Eta model. Preprints, *15th Conf. on Numerical Weather Prediction*, San Antonio, TX, Amer. Meteor. Soc., 280–283.
- Fiorino, M. J., and R. L. Elsberry, 1989: Some aspects of vortex structure related to tropical cyclone motion. *J. Atmos. Sci.*, **46**, 975–990.
- Fovell, R. G., and H. Su, 2007: Impact of cloud microphysics on hurricane track forecasts. *Geophys. Res. Lett.*, **34**, L24810, doi:10.1029/2007GL031723.
- , K. L. Corbosiero, and H.-C. Kuo, 2009: Cloud microphysics impact on hurricane track as revealed in idealized experiments. *J. Atmos. Sci.*, **66**, 1764–1778.
- , —, A. Seifert, and K. N. Liou, 2010a: Impact of cloud-radiative processes on hurricane track. *Geophys. Res. Lett.*, **37**, L07808, doi:10.1029/2010GL042691.
- , —, and H.-C. Kuo, 2010b: Influence of cloud-radiative feedback on tropical cyclone motion: Symmetric contributions. Preprints, *29th Conf. on Hurricanes and Tropical Meteorology*, Tucson, AZ, Amer. Meteor. Soc., 13C.5. [Available online at <https://ams.confex.com/ams/pdfpapers/168859.pdf>.]
- Frank, W. M., and E. A. Ritchie, 1999: Effects of environmental flow upon tropical cyclone structure. *Mon. Wea. Rev.*, **127**, 2044–2061.
- Fudeyasu, H., and Y. Wang, 2011: Balanced contribution to the intensification of a tropical cyclone simulated in TCM4: Outer-core spinup process. *J. Atmos. Sci.*, **68**, 430–449.
- Gopalakrishnan, S. G., S. Goldenberg, T. Quirino, X. Zhang, F. Marks, K.-S. Yeh, R. Atlas, and V. Tallapragada, 2012: Toward improving high-resolution numerical hurricane forecasting: Influence of model horizontal grid resolution, initialization, and physics. *Wea. Forecasting*, **27**, 647–666.
- Gray, W. M., and R. W. Jacobson, 1977: Diurnal variation of deep cumulus convection. *Mon. Wea. Rev.*, **105**, 1171–1188.
- Hack, J. J., and W. H. Schubert, 1986: Nonlinear response of atmospheric vortices to heating by organized cumulus convection. *J. Atmos. Sci.*, **43**, 1559–1573.
- Hill, K. A., and G. M. Lackmann, 2009: Influence of environmental humidity on tropical cyclone size. *Mon. Wea. Rev.*, **137**, 3294–3315.
- Holland, G. J., 1983: Tropical cyclone motion: Environmental interaction plus a beta effect. *J. Atmos. Sci.*, **40**, 328–342.
- , and R. T. Merrill, 1984: On the dynamics of tropical cyclone structural changes. *Quart. J. Roy. Meteor. Soc.*, **110**, 723–745.
- Houze, R. A., 2010: Clouds in tropical cyclones. *Mon. Wea. Rev.*, **138**, 293–344.
- Iacono, M. J., J. S. Delamere, E. J. Mlawer, M. W. Shephard, S. A. Clough, and W. D. Collins, 2008: Radiative forcing by long-lived greenhouse gases: Calculations with the AER radiative transfer models. *J. Geophys. Res.*, **113**, D13103, doi:10.1029/2008JD009944.
- Janjić, Z. I., 2003: A nonhydrostatic model based on a new approach. *Meteor. Atmos. Phys.*, **82** (1–4), 271–285, doi:10.1007/s00703-001-0587-6.
- Jordan, C. L., 1958: Mean soundings for the West Indies area. *J. Meteor.*, **15**, 91–97.
- Lin, N., and D. Chavas, 2012: On hurricane parametric wind and applications in storm surge modeling. *J. Geophys. Res.*, **117**, D09120, doi:10.1029/2011JD017126.
- Lord, S. J., H. E. Willoughby, and J. M. Piotrowicz, 1984: Role of a parameterized ice-phase microphysics in an axisymmetric, nonhydrostatic tropical cyclone model. *J. Atmos. Sci.*, **41**, 2836–2848.
- Rotunno, R., and K. A. Emanuel, 1987: An air–sea interaction theory for tropical cyclones. Part II: Evolutionary study using a nonhydrostatic axisymmetric numerical model. *J. Atmos. Sci.*, **44**, 542–561.
- Rozoff, C. M., D. S. Nolan, J. P. Kossin, F. Zhang, and J. Fang, 2012: The roles of an expanding wind field and inertial stability in tropical cyclone secondary eyewall formation. *J. Atmos. Sci.*, **69**, 2621–2643.
- Schubert, W. H., and J. J. Hack, 1982: Inertial stability and tropical cyclone development. *J. Atmos. Sci.*, **39**, 1687–1697.
- Shapiro, L. J., and H. E. Willoughby, 1982: The response of balanced hurricanes to local sources of heat and momentum. *J. Atmos. Sci.*, **39**, 378–394.
- Tang, B., and K. A. Emanuel, 2012: Sensitivity of tropical cyclone intensity to ventilation in an axisymmetric model. *J. Atmos. Sci.*, **69**, 2394–2413.
- Thompson, G., P. R. Field, R. M. Rasmussen, and W. D. Hall, 2008: Explicit forecasts of winter precipitation using an improved bulk microphysics scheme. Part II: Implementation of a new snow parameterization. *Mon. Wea. Rev.*, **136**, 5095–5115.
- Wang, Y., 2002: An explicit simulation of tropical cyclones with a triply nested movable mesh primitive equation model: TCM3. Part II: Model refinements and sensitivity to cloud microphysics parameterization. *Mon. Wea. Rev.*, **130**, 3022–3036.
- , 2009: How do outer spiral rainbands affect tropical cyclone structure and intensity? *J. Atmos. Sci.*, **66**, 1250–1273.
- Weatherford, C. L., and W. M. Gray, 1988a: Typhoon structure as revealed by aircraft reconnaissance. Part I: Data analysis and climatology. *Mon. Wea. Rev.*, **116**, 1032–1043.
- , and —, 1988b: Typhoon structure as revealed by aircraft reconnaissance. Part II: Structural variability. *Mon. Wea. Rev.*, **116**, 1044–1056.
- Willoughby, H. E., 1979: Forced secondary circulations in hurricanes. *J. Geophys. Res.*, **84** (C6), 3173–3183.
- , F. D. Marks, and R. J. Feinberg, 1984: Stationary and moving convective bands in hurricanes. *J. Atmos. Sci.*, **41**, 3189–3211.
- Xu, J., and Y. Wang, 2010a: Sensitivity of tropical cyclone inner-core size and intensity to the radial distribution of surface entropy flux. *J. Atmos. Sci.*, **67**, 1831–1852.
- , and —, 2010b: Sensitivity of the simulated tropical cyclone inner-core size to the initial vortex size. *Mon. Wea. Rev.*, **138**, 4135–4157.
- Zhu, T., and D.-L. Zhang, 2006: Numerical simulation of Hurricane Bonnie (1998). Part II: Sensitivity to varying cloud microphysical processes. *J. Atmos. Sci.*, **63**, 109–126.